REPORT DOCUMENTATION PAGE		Form Approved OMB NO. 0704-0188

1. REPORT DATE (DD-MM-YYYY)	2. REPORT TYPE	3. DATES COVERED (From - To)
	New Reprint	-

4. TITLE AND SUBTITLE	5a. CONTRACT NUMBER
Reversible Strain-Induced Electron–Hole Recombination in Silicon Nanowires Observed with Femtosecond Pump–Probe Microscopy	
	5b. GRANT NUMBER
	W911NF-04-D-0004
	5c. PROGRAM ELEMENT NUMBER
	611102

6. AUTHORS	5d. PROJECT NUMBER
Erik M. Grumstrup, Michelle M. Gabriel, Christopher W. Pinion, James K. Parker, James F. Cahoon, John M. Papanikolas	
	5e. TASK NUMBER
	5f. WORK UNIT NUMBER

7. PERFORMING ORGANIZATION NAMES AND ADDRESSES	8. PERFORMING ORGANIZATION REPORT NUMBER
University of North Carolina - Chapel Hill 104 Airport Drive Suite 2200 Chapel Hill, NC 27599 -1350	

9. SPONSORING/MONITORING AGENCY NAME(S) AND ADDRESS (ES)	10. SPONSOR/MONITOR'S ACRONYM(S)
U.S. Army Research Office P.O. Box 12211 Research Triangle Park, NC 27709-2211	ARO
	11. SPONSOR/MONITOR'S REPORT NUMBER(S)
	58087-CH-SR.4

12. DISTRIBUTION AVAILIBILITY STATEMENT
Approved for public release; distribution is unlimited.

13. SUPPLEMENTARY NOTES
The views, opinions and/or findings contained in this report are those of the author(s) and should not contrued as an official Department of the Army position, policy or decision, unless so designated by other documentation.

14. ABSTRACT

Strain-induced changes to the electronic structure of nanoscale materials provide a promising avenue for expanding the optoelectronic functionality of semiconductor nanostructures in device applications. Here we use pump–probe microscopy with femtosecond temporal resolution and submicron spatial resolution to characterize charge–carrier recombination and transport dynamics in silicon nanowires (NWs) locally strained by bending deformation. The electron–hole recombination rate increases with strain for values above a threshold of ?1% and, in highly strained (≥5%) regions of the NW, increases 6-fold. The changes in recombination rate are independent of NW diameter and

15. SUBJECT TERMS
Ultrafast imaging, strained nanomaterials, spectroscopy

16. SECURITY CLASSIFICATION OF:			17. LIMITATION OF ABSTRACT	15. NUMBER OF PAGES	19a. NAME OF RESPONSIBLE PERSON
a. REPORT	b. ABSTRACT	c. THIS PAGE			James Parker
UU	UU	UU	UU		19b. TELEPHONE NUMBER
					919-549-4293

Report Title

Reversible Strain-Induced Electron–Hole Recombination in Silicon Nanowires Observed with Femtosecond Pump–Probe Microscopy

ABSTRACT

Strain-induced changes to the electronic structure of nanoscale materials provide a promising avenue for expanding the optoelectronic functionality of semiconductor nanostructures in device applications. Here we use pump–probe microscopy with femtosecond temporal resolution and submicron spatial resolution to characterize charge–carrier recombination and transport dynamics in silicon nanowires (NWs) locally strained by bending deformation. The electron–hole recombination rate increases with strain for values above a threshold of ?1% and, in highly strained (? 5%) regions of the NW, increases 6-fold. The changes in recombination rate are independent of NW diameter and reversible upon reduction of the applied strain, indicating the effect originates from alterations to the NW bulk electronic structure rather than introduction of defects. The results highlight the strong relationship between strain, electronic structure, and charge–carrier dynamics in low-dimensional semiconductor systems, and we anticipate the results will assist the development of strain-enabled optoelectronic devices with indirect-bandgap materials such as silicon.

REPORT DOCUMENTATION PAGE (SF298)
(Continuation Sheet)

Continuation for Block 13

ARO Report Number   58087.4-CH-SR
Reversible Strain-Induced Electron–Hole Recon...

Block 13: Supplementary Note

Reversible Strain-Induced Electron−Hole Recombination in Silicon Nanowires Observed with Femtosecond Pump−Probe Microscopy

Erik M. Grumstrup,*[†,‡] Michelle M. Gabriel,[†] Christopher W. Pinion,[†] James K. Parker,[‡] James F. Cahoon,*[†] and John M. Papanikolas*[†]

[†]Department of Chemistry, University of North Carolina at Chapel Hill, Chapel Hill, North Carolina 27599, United States
[‡]Chemical Sciences Division, US Army Research Office, P.O. Box 12211, Research Triangle Park, North Carolina 27709, United States

Ⓢ *Supporting Information*

ABSTRACT: Strain-induced changes to the electronic structure of nanoscale materials provide a promising avenue for expanding the optoelectronic functionality of semiconductor nanostructures in device applications. Here we use pump−probe microscopy with femtosecond temporal resolution and submicron spatial resolution to characterize charge−carrier recombination and transport dynamics in silicon nanowires (NWs) locally strained by bending deformation. The electron−hole recombination rate increases with strain for values above a threshold of ∼1% and, in highly strained (∼5%) regions of the NW, increases 6-fold. The changes in recombination rate are independent of NW diameter and reversible upon reduction of the applied strain, indicating the effect originates from alterations to the NW bulk electronic structure rather than introduction of defects. The results highlight the strong relationship between strain, electronic structure, and charge−carrier dynamics in low-dimensional semiconductor systems, and we anticipate the results will assist the development of strain-enabled optoelectronic devices with indirect-bandgap materials such as silicon.

KEYWORDS: Ultrafast imaging, strained nanomaterials, spectroscopy
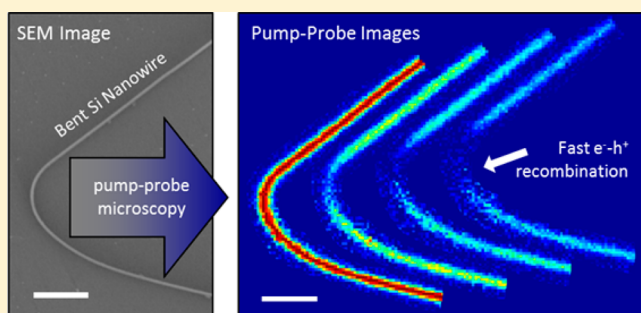
Lattice strain produced by bending deformation can significantly alter material properties, such as band energies, symmetry, and carrier mobility, providing the potential means to develop novel functionalities in nanoscale devices.[1−5] In Si nanowires (NWs), for example, strain may offer a route toward Si lasers and light-emitting diodes (LEDs),[6] enhanced carrier transport in nanoscale electronics,[7−9] and junctionless charge separation in Si NW-based photovoltaics.[10] The potential for accessing such unique functionalities has prompted both experimental[11−16] and theoretical[4,6−10,17,18] studies of materials under high levels (>2%) of both homogeneous and inhomogeneous strain. Spectroscopic methods provide direct insight into the influence of lattice strain on the electronic structure. For example, strain-induced redshifts in the emission spectra of bent ZnO[11−14] and CdSe[15] NWs observed using fluorescence microscopy indicate that lattice strain can significantly reduce the band gap, and cathodoluminescence measurements of ZnO NWs suggest excitons tend to drift from regions of compressive strain (with larger bandgap) toward regions of tensile strain (with smaller bandgap) at cryogenic temperatures.[16] While strain has a clear impact on the electronic structure of nanomaterials, its influence on the carrier dynamics (e.g., carrier lifetime and mobility) remains largely unexplored, particularly in indirect-

bandgap materials such as Si and Ge that cannot be studied using luminescent techniques.

Here we present time-resolved pump−probe microscopy[19−23] measurements of the photoexcited charge carrier dynamics in individual Si NWs that are inhomogeneously strained through bending deformation. The combination of submicron spatial resolution and femtosecond temporal resolution, as well as the ability to control the position of the probe beam relative to the pump beam, enables direct measurement of both charge carrier diffusion constants and electron−hole recombination rates at localized points along straight and bent regions of individual NWs. Decay kinetics collected at 144 discrete locations within 14 different NWs show a clear correlation between the electron−hole recombination rate and the degree of lattice strain, with NWs exhibiting up to a 6-fold increase of the carrier recombination rate in regions experiencing the highest strain (∼5%). By studying NWs on flexible polydimethylsiloxane (PDMS) substrates, we further show the changes in the recombination rate are reversible, indicating that the intrinsic electronic structure of

low dimensional semiconductor systems can be manipulated by straining the lattice without introducing defects.

In these experiments, photoexcited carriers are created in a localized region of a single NW by a femtosecond laser pulse (pump: 425 nm, 0.4 pJ/pulse, 300 μJ/cm^2) that is focused to a near diffraction-limited spot by a microscope objective (100×, NA = 0.8). The spatial and temporal evolution of the photogenerated carriers are followed by a second laser pulse (probe: 850 nm, 150 μJ/cm^2) that is also focused by the objective. Pump-induced changes in the intensity of probe pulses are monitored by collecting the probe light transmitted through the sample and directing it onto a two-channel balanced photodetector coupled to a digital lock-in amplifier. The probe beam can be laterally positioned relative to the pump spot by adjusting the angle of incidence at the back aperture of the microscope objective using a pair of computer-controlled mirrors. The spatial evolution of the photoexcited carrier density is monitored by scanning the probe position on a pixel-by-pixel basis relative to the pump at a fixed pump–probe temporal delay time, Δt. The microscope is capable of measuring the carrier dynamics in a localized region of a single structure with spatial resolution of ~700 nm and a temporal resolution of ~500 fs.[21−23]

Intrinsic Si NW samples were synthesized by the vapor–liquid–solid (VLS) mechanism at 420 °C using Au catalysts for VLS growth in a low-pressure chemical vapor deposition system under conditions identical to those described previously.[24] NWs were thermally oxidized at 1000 °C for 60 s in 100 Torr flowing oxygen to form a 5−10 nm-thick thermal oxide and were mechanically transferred from the growth substrates to microscopy slides for imaging. The scanning electron microscopy (SEM) image of a typical ~100 nm diameter Si NW (denoted NW1) that was bent during the transfer from the growth substrate to a microscope slide is shown in Figure 1A. Although the lattice in the straight segments of the NW is under little external stress, the bent region experiences compression and tension on the inner and outer edges, respectively.

Microscopy measurements performed with spatially over-lapped pump and probe pulses show distinct decay kinetics in the straight segments compared to the bent segments. The decay kinetics obtained at the seven different locations along NW1 (indicated by the corresponding circles in panel A) are displayed in Figure 1B. At all seven locations, there is an initial increase in probe transmittance that reflects the population of free carriers produced by photoexcitation.[22,25] The decay of the signal reflects recombination of electrons and holes, which under low-strain conditions (blue traces) occurs primarily at the surface. In the regions of high curvature (red and green traces), the electron–hole recombination is faster, with the higher-curvature points in red decaying more quickly than the lower-curvature point in green.

Spatial variation in carrier recombination can be visualized in pump–probe images (Figure 1C). Here, the pump–probe delay is fixed, and the focused pump and probe beams are scanned over the structure to produce a spatial map of the transient signal at a specific delay time. The raw ("as collected") images obtained in this manner generally show a spatial variation in the signal intensity that stems from a dependence of the absorption and scattering cross sections on the laser beam polarizations. Even though the magnitude of the transient signal is diminished in regions where the wire is oriented orthogonal to the polarization axis, the kinetics are not
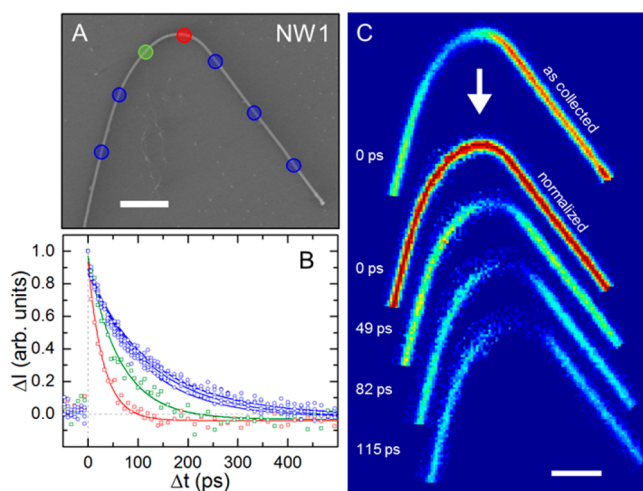

Figure 1. Charge carrier recombination in a Si NW locally strained by a bending deformation (A) SEM image of a bent Si nanowire ~100 nm in diameter (NW1). Colored circles denote regions where transient kinetics were acquired; scale bar, 2 μm. (B) Normalized kinetic traces of carrier recombination dynamics collected at multiple locations on NW1. Red, green, and blue data points correspond to the locations denoted by red, green, and blue circles in panel A, respectively. Solid lines correspond to a fit of each kinetic trace to eq 1. (C) Sequence of spatially overlapped pump–probe images from NW1 in panel A, showing faster carrier recombination near the bent, high-strain region. The upper image depicts the raw ("as collected") data, whereas the bottom four images are normalized relative to the data at Δt = 0 ps; scale bar, 2 μm.

affected.[22] The images in the lower portion of Figure 1C have been normalized to remove this spatial variation, resulting in a constant signal intensity along the NW at Δt = 0 ps. As the delay between pump and probe pulses is increased, the signal in the bent region of the NW fades quickly compared to the straight segments, consistent with faster electron–hole recombination. Closer inspection of the images indicates that the increase in the recombination rate varies continuously along the bend, with the region of highest curvature showing the fastest recombination. The discussion below expands upon this qualitative observation by providing a quantitative correlation between the recombination rate and degree of NW curvature.

Electron–hole recombination rates were determined by fitting kinetic traces, such as those depicted in Figure 1B, to a previously developed model of diffusion and recombination[22] consisting of a single-exponential function modified to account for the size of the pump and probe beams as well as carrier diffusion out of the probe volume:

$$I(\Delta t, \Delta x) = \frac{a_0}{\beta(\Delta t)} \exp\left(\frac{-4\ln(2)\Delta x^2}{\beta(\Delta t)^2}\right) \exp(-k_{obs}\Delta t)$$

(1)

with

$$\beta(\Delta t)^2 = \gamma_1^2 + \gamma_2^2 + 16\ln(2)D\Delta t$$

(2)

In eq 1, Δx defines the spatial separation between pump and probe spots along the wire (Δx = 0 for these spatially overlapped kinetics traces), a_0 is a normalization constant, and k_{obs} is the electron–hole recombination rate. In eq 2, γ_1 = 430 nm and γ_2 = 860 nm are the full-width at half-maximums (FWHMs) of the pump and probe spots, and D is the effective ambipolar diffusion constant of the material.
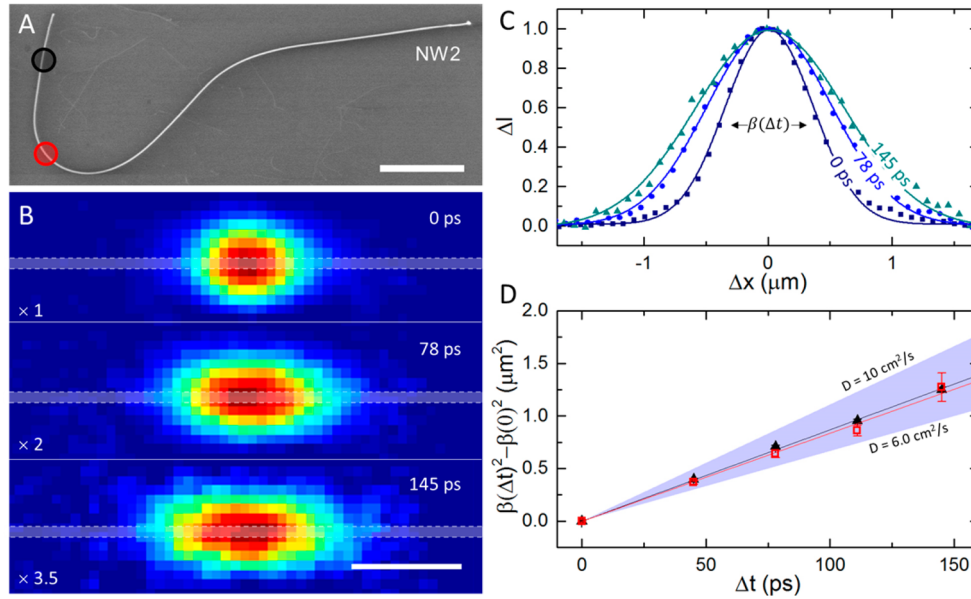
Figure 2. Charge carrier diffusion in a Si NW locally strained by a bending deformation (A) SEM image of a bent Si nanowire ~100 nm in diameter (NW2); scale bar, 5 μm. (B) Spatially separated pump−probe images of carrier diffusion at the location indicated by the black circle in panel A. Dashed white lines denote the location of the NW; scale bar, 1 μm. (C) Normalized carrier profiles obtained by integrating the spatially separated images shown in panel B in the direction orthogonal to carrier diffusion. Data are shown as symbols, and solid lines represent fits of the data to eq 3. (D) Change in the square of the carrier profile fwhm, $\beta(\Delta t)^2 - \beta(0)^2$, as a function of pump−probe delay for bent (red square) and straight (black triangle) locations indicated by the red and black circles, respectively, in panel A. The blue shaded region shows the range of diffusion constants (6.0 cm^2/s < D < 10.0 cm^2/s) found for four additional NWs characterized.

The diffusion constant is determined using the spatially separated pump−probe microscopy configuration that allows direct and contactless characterization of the transport properties. Figure 2A shows an SEM image of a single bent Si NW (NW2) with black and red circles indicating straight and bent regions, respectively, where carrier transport was characterized. In Figure 2B, spatially separated pump−probe images obtained from the straight region at Δt = 0, 78, and 145 ps show progressive broadening of the photogenerated charge cloud as a result of carrier diffusion.

Normalized carrier profiles, generated by integrating the images along the direction normal to the NW axis, are shown in Figure 2C. These profiles are fit to the spatially dependent terms of eq 1:

$$I'(\Delta t, \Delta x) = \frac{a_0}{\beta(\Delta t)} \exp\left(\frac{-4 \ln(2) \Delta x^2}{\beta(\Delta t)^2}\right) \qquad (3)$$

to extract the fwhm of the distribution, $\beta(\Delta t)$. A plot of $\beta(\Delta t)^2$ as a function of pump−probe delay yields a linear relationship with a slope that is proportional to the diffusion constant, D, and a y-intercept, $\beta(0)$, that reflects the pump and probe spot sizes (see eq 2 for Δt = 0 ps). Figure 2D shows the time-dependent component of the fwhm, $(\beta(\Delta t)^2 - \beta(0)^2)$, for the bent and straight regions of NW2. Analysis of this data yielded diffusion constants of 7.5 ± 0.2 cm^2/s and 7.8 ± 0.1 cm^2/s, respectively, for the two regions. Characterization of carrier transport in four additional NWs yielded diffusion constants that ranged from 6 cm^2/s and 10 cm^2/s with no apparent correlation between the local curvature and the diffusion constant. The average diffusion constant found for these NWs (~8 cm^2/s) is significantly lower than the bulk ambipolar diffusion constant of 18 cm^2/s,[26] which is most likely a consequence of the high photoexcited carrier density (~4 ×

10^{19} cm^{-3}) dominating transport through carrier−carrier scattering.[27]

Although lattice strain is anticipated to affect charge carrier mobility,[7−9,17] the lack of a strain dependence in our measurements may be a consequence of several factors. First, in Si, the electron mobility (μ_e) is typically increased in regions under tensile strain and decreased under compression, with the opposite behavior expected for the hole mobility (μ_h). Since the ambipolar diffusion constant depends upon both (i.e., $D = (2k_BT/q)(\mu_e\mu_h/\mu_e + \mu_h)$, where k_B is the Boltzmann constant, T is temperature, and q is elementary charge), an increase in the electron mobility could be partially offset by a decrease in hole mobility, resulting in very little difference in the measured ambipolar diffusion constant. In addition, a strain dependence may be masked by the diffraction-limited spatial averaging that samples both compressive (at the inside edge) and tensile (at the outside edge) strain of the bent NW (see Figure 4 and discussion below). In this case, minimal impact on the transport properties arising from strain would be apparent.

Electron−hole recombination times were determined by fitting the kinetic traces shown in Figure 1B to eq 1 with D = 8 cm^2/s. This analysis yielded recombination times of ~150 ps in the straight segments (blue circles) and 72 and 33 ps at the bent regions indicated by the green and red circles, respectively, in Figure 1A. Although we used an average carrier diffusion constant of 8 cm^2/s for fitting the kinetic traces, fits conducted with values of D from 6 to 10 cm^2/s changed the extracted rates by less than 15%.

The simplest explanation for the increase in the recombination rate in the regions of higher curvature is an increase in the trap density due to bond breaking or dislocation effects in the crystal lattice or at the surface.[18,19] The creation of defect sites would likely be irreversible, causing rapid recombination to persist even after release of the deformation. To test this idea,
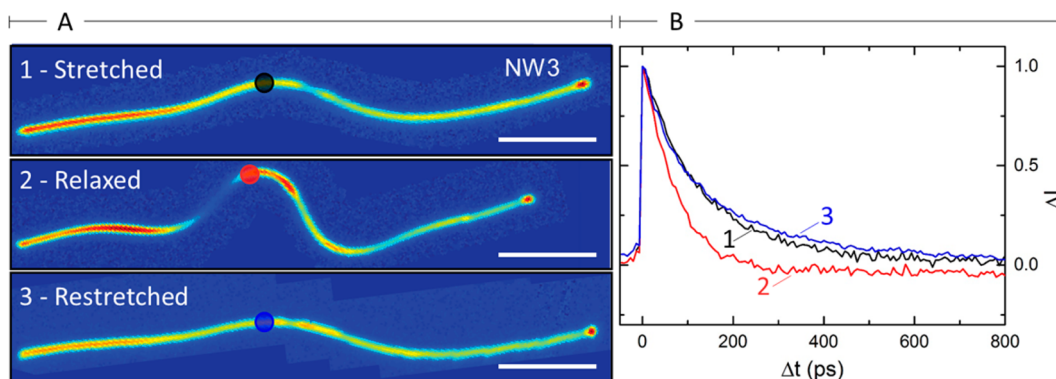
C

Figure 3. Reversibility of the strain-dependent carrier recombination rate. (A) Pump−probe images at $\Delta t = 0$ for NW3 ($d \sim 100$ nm) deposited on a flexible PDMS substrate in initial stretched (1), relaxed (2), and restretched (3) configurations; scale bars, 5 μm. (B) Transient kinetic traces collected from the same position (indicated by circles in panel A) along the length of NW3 in its initial straight (1), bent (2), and straightened (3) configurations.

we investigated carrier recombination dynamics in NWs transferred to a stretched poly(dimethylsiloxane) (PDMS) substrate. The pump−probe image taken at $\Delta t = 0$ ps for a single Si nanowire (NW3) in its initial straight configuration is shown in panel 1 of Figure 3A. The electron−hole recombination time (Figure 3B) observed at the point indicated by the black circle is similar to those observed in the low curvature regions of NW1. The substrate was then allowed to relax, and NW3 adopted a bent configuration (panel 2). The rate of recombination at a corresponding position along NW3 (red circle) increases, commensurate with the higher-curvature regions of NW1. Finally, the substrate was restretched (panel 3), and NW3 returned to its initial straight configuration. Once the deformation was released, recombination slowed, returning to its prebent character. This reversible behavior suggests that the changes in the recombination kinetics observed in regions of higher curvature are not the result of an increase in defect density but rather stem from an intrinsic change in the energetics or symmetry of NW band structure due to elastic deformation of the lattice.

The strain induced by elastic deformation of a NW from bending can be analytically determined from the local radius of curvature, R (Figure 4A). The strain in this configuration consists of a gradual shift from lattice compression at the inner edge to lattice tension at the outer edge and has a maximum magnitude, $|\varepsilon|$, that can be expressed in terms of R and the NW diameter, d, as $|\varepsilon| = d/2R$ (see Figure 4B). For the locations indicated by the blue circles in NW1 (Figure 1A), the calculated strain is less than 1%, and the observed electron−hole recombination rate, k_{obs}, is between 6 and 8 ns^{-1}. The regions of higher curvature (green and red circles in Figure 1A) on the NW have $|\varepsilon| = 1.9\%$ ($k_{obs} = 13.8$ ns^{-1}) and $|\varepsilon| = 2.7\%$ ($k_{obs} = 30.3$ ns^{-1}), respectively. This corresponds to enhancement factors of ~ 2 at 2% strain and 4−5 at 3% strain. Given the lateral resolution of the microscope, k_{obs} is a spatial average of the carrier recombination dynamics that encompasses regions experiencing both tension and compression. As a result of this spatial averaging, the observed rate reflects the average of the carrier recombination dynamics throughout the NW.

Multiple electron−hole recombination mechanisms are potentially present in NWs, producing an observed recombination rate that is the sum of bulk and surface processes:
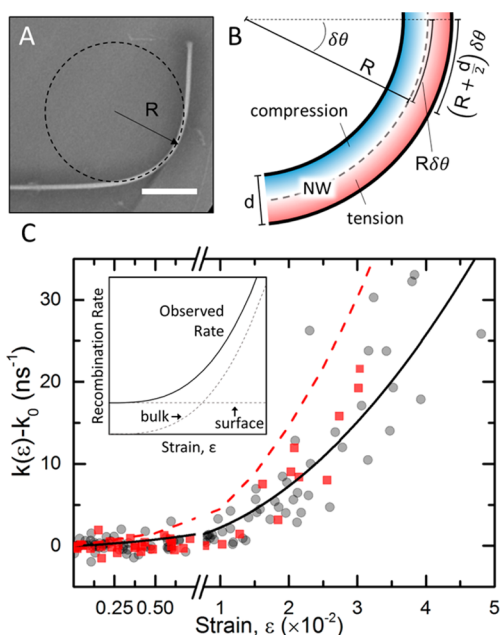
$$k_{obs} = k_s + k_r + k_{SRH} + k_A \qquad (4)$$

Figure 4. Correlation between carrier recombination rate and lattice strain. (A) SEM image of a bent Si NW (~ 100 nm in diameter) illustrating the local radius of curvature, R. The scale bar is 1 μm. (B) Schematic showing the regions of compression (shaded blue) and tension (shaded red) predicted in a bent NW. (C) Combined strain dependence of the carrier recombination rate for 14 individual NWs. R was determined for each measurement through analysis of the NW transmission images, and the diameter was determined from SEM images. NWs grown with 100 nm Au catalysts (gray circles) and 50 nm Au catalysts (red squares) show the same trend. The black solid line is a quadratic trend line fit to the 100 nm rates. Red dashed line shows behavior predicted for 50 nm NWs if strain-dependent rate contributions were a surface effect. Inset: illustration of surface and bulk contributions to the overall electron−hole recombination rate as a function of strain.

where k_s, k_r, k_{SRH}, and k_A represent the rates associated with surface, radiative, Shockley−Read−Hall (SRH), and Auger recombination, respectively. Previous work in our lab showed that recombination in straight NW segments takes place at the surface and is well-described by $k_s = 4S/d$, where the surface recombination velocity (S) parametrizes the surface quality.[21,22,25] The inverse diameter dependence in this expression reflects the geometrical localization of recombination events to

the surface. In these low-dimensional NWs, radiative and SRH recombination mechanisms do not compete with surface recombination, which is orders of magnitude faster at room temperature.[25,28,29] Auger recombination can also contribute to the observed rate; however, the pump−probe decays are independent of the pump pulse energies below 0.4 pJ/pulse, in both bent and straight regions of individual NWs (Figure S1), indicating that at the excitation energies of these experiments, Auger processes are not a major contributor (i.e., $k_A \approx 0$).

The increase in recombination rate upon bending deformation could arise from a strain-induced enhancement of one or more of these mechanisms. Thus, the observed electron−hole recombination rate can be expressed as a sum of strain-independent (k_0) and strain-dependent ($k(\varepsilon)$) contributions:

$$k_{obs} = k_0 + k(\varepsilon) \tag{5}$$

The strain-dependent component, $k(\varepsilon) = k_{obs} - k_0$, is plotted in Figure 4C for 144 measurements across 14 different wires. Due to differences in surface quality and diameter, we determined k_0 on a NW-by-NW basis by averaging the low strain (<0.5%) recombination rates found for each individual NW. It appears that the carrier recombination rate is independent of strain up to a value of ∼0.7%, at which point the strain-dependent contribution begins to influence the overall recombination dynamics.

Although the reversibility of the strain-dependent recombination suggests an intrinsic change to the band structure, the reversibility alone is insufficient to determine if the change in recombination results from a process in the core of the NW or at the surface, due, for example, to changes in the coupling between the bulk bands and the surface states. Nevertheless, these two scenarios can be distinguished by examining NWs of different diameters. If surface recombination (k_s) is increased by lattice strain, then the strain dependence should scale inversely with NW diameter (since $k_s = 4S/d$). The black line in Figure 4C is a quadratic trend line fit to the ∼100 nm NW data. If the strain effect is occurring at the surface, then recombination rates collected from ∼50 nm wires should lie along the dashed red line (which shows a 2-fold greater strain variation due to the 2-fold difference in diameter). This is not the case. Strain-dependent recombination rates collected from ∼50 nm diameter wires (shown as red squares in Figure 4C) follow a similar trend as the ∼100 nm diameter NWs. Although there is some spread in the data, the strain-dependent rates appear inconsistent with a surface recombination model, suggesting that the strain-induced increase in the rate, $k(\varepsilon)$, is primarily a consequence of recombination events that are occurring throughout the NW volume.

The dependence of the electron−hole recombination rate on strain is illustrated in the inset of Figure 4C. At low strain ($\varepsilon <$ 0.7%), recombination via typical bulk mechanisms (i.e., SRH, Auger, radiative) is slow, and the overall recombination is dominated by the surface (i.e., $k_{obs} \approx k_0 = k_s$). Lattice strain introduced by bending deformation enhances the bulk recombination rate, and at $\varepsilon \sim$ 0.7%, the strain-induced enhancement in the bulk recombination rate has a noticeable impact on the overall rate. By 4−5% strain, it dominates the recombination process. Even though it is unclear which specific bulk mechanism (SRH or, radiative) is affected, in either case, the increase likely arises from strain-induced changes to the Si band structure that include a reduced band gap or, in the case

of the inhomogeneous strain (such as that produced by bending deformation), a change to the symmetry of the lattice.

A number of mechanisms may be at play in determining the carrier recombination kinetics in bent NWs. Calculations performed by other groups on strained Si predict that the bandgap can be reduced by as much as 0.5 eV at 4−5% strain, suggesting that faster recombination may occur through improved energetic overlap of the photogenerated carriers with the manifold of trap states.[6,7,10,30] However, it is also predicted[10] that the conduction and valence band energies are both stabilized in regions of tensile strain, and they are both increased in energy in regions of compressive strain. Thus, in the neighborhood of a bend, a potential gradient should exist across the NW that would serve to rapidly separate electrons and holes, lengthening the charge carrier lifetime in the region of a bend. The absence of this behavior in the strain-dependent rate constant may stem from the high density of photo-generated carriers, which could screen the effects of the strain-induced potential in a manner analogous to recent measurements made by our group of a P−I−N junction.[23] Efforts directed toward reducing the photoexcited carrier density and improving spatial resolution (to possibly image charge separation in a bent NW) are currently underway. In addition to energetic effects, calculations also show dramatic changes to the band symmetry occur with increasing strain, resulting in a loss of the indirect band gap character.[6,7,10,30] Because electron−hole recombination events in indirect semiconductors (e.g., unstrained Si) typically require the emission of multiple phonons to span the energy and momentum difference between conduction and valence band electrons,[31] this rearrangement of the electronic structure may mitigate the momentum mismatch and accelerate both SRH and radiative electron−hole recombination.

In summary, we have observed carrier recombination rates in bent Si NWs that are nearly 6-fold higher than straight Si NWs. The enhancement is reversible, with bent wires recovering their unstrained carrier decay kinetics when they are straightened. The observations are consistent with elastic strain-induced changes to the intrinsic electronic structure of NWs, whereby a reduction in the band gap energy and alteration of conduction and valence band symmetry causes faster free carrier recombination. These results have important implications for a broad range of Si-based devices, in which changes to the fundamental material properties of Si make strain a tool for achieving novel functionality in electronic and optoelectronic devices. Although promising, the peripheral effects of strain in Si, particularly the enhanced carrier recombination rate, may be problematic to the efficient operation of these devices, especially optoelectronic devices that rely on long charge carrier lifetimes, such as nanostructured solar cells. Further studies of the effects of strain on the carrier dynamics of silicon (and other material) nanostructures, particularly in architectures amenable to device applications (uniaxial, biaxial strained NWs), will be important indicators for the development of strained NW technologies.

■ ASSOCIATED CONTENT

Ⓢ Supporting Information

Power-dependent kinetics for both bent and straight regions of a Si NW. This material is available free of charge via the Internet at http://pubs.acs.org.

■ AUTHOR INFORMATION

Corresponding Authors
*E-mail: E.M.G. (erik.grumstrup@montana.edu).
*E-mail: J.F.C. (jfcahoon@unc.edu).
*E-mail: J.M.P. (john_papanikolas@unc.edu).

Present Address
E.M.G.: Department of Chemistry and Biochemistry, Montana State University, Bozeman, MT 59717.

Notes
The authors declare no competing financial interest.

■ ACKNOWLEDGMENTS

■ REFERENCES

(1) Smith, A. M.; Mohs, A. M.; Nie, S. *Nat. Nanotechnol.* **2009**, *4* (1), 56−63.

(2) Sun, Y. T.; Scott, E.; Toshikazu, N. *Strain Effect in Semiconductors*; Springer: New York, 2010.

(3) Suess, M. J.; Geiger, R.; Minamisawa, R. A.; Schiefler, G.; Frigerio, J.; Chrastina, D.; Isella, G.; Spolenak, R.; Faist, J.; Sigg, H. *Nat. Photonics* **2013**, *7* (6), 467−473.

(4) Li, J.; Shan, Z.; Ma, E. *MRS Bull.* **2014**, *39* (02), 108−114.

(5) Priolo, F.; Gregorkiewicz, T.; Galli, M.; Krauss, T. F. *Nat. Nanotechnol.* **2014**, *9* (1), 19−32.

(6) Shiri, D.; Verma, A.; Selvakumar, C. R.; Anantram, M. P. *Sci. Rep.* **2012**, *2*, 461.

(7) Shiri, D.; Kong, Y.; Buin, A.; Anantram, M. P. *Appl. Phys. Lett.* **2008**, *93* (7), 073114.

(8) Niquet, Y. M.; Delerue, C.; Krzeminski, C. *Nano Lett.* **2012**, *12* (7), 3545−50.

(9) Nguyen, V. H.; Triozon, F.; Bonnet, F. D. R.; Niquet, Y. M. *IEEE Trans. Electron Devices* **2013**, *60* (5), 1506−1513.

(10) Wu, Z.; Neaton, J. B.; Grossman, J. C. *Nano Lett.* **2009**, *9* (6), 2418−22.

(11) Xue, H.; Pan, N.; Li, M.; Wu, Y.; Wang, X.; Hou, J. G. *Nanotechnology* **2010**, *21* (21), 215701.

(12) Xu, S.; Guo, W.; Du, S.; Loy, M. M.; Wang, N. *Nano Lett.* **2012**, *12* (11), 5802−7.

(13) Wei, B.; Zheng, K.; Ji, Y.; Zhang, Y.; Zhang, Z.; Han, X. *Nano Lett.* **2012**, *12* (9), 4595−9.

(14) Han, X.; Kou, L.; Zhang, Z.; Zhang, Z.; Zhu, X.; Xu, J.; Liao, Z.; Guo, W.; Yu, D. *Adv. Mater.* **2012**, *24* (34), 4707−4711.

(15) Sun, L.; Kim do, H.; Oh, K. H.; Agarwal, R. *Nano Lett.* **2013**, *13* (8), 3836−42.

(16) Fu, X.; Jacopin, G.; Shahmohammadi, M.; Liu, R.; Benameur, M.; Ganiere, J. D.; Feng, J.; Guo, W.; Liao, Z. M.; Deveaud, B.; Yu, D. *ACS Nano* **2014**, *8* (4), 3412−20.

(17) Richard, S.; Aniel, F. d. r.; Fishman, G.; Cavassilas, N. *J. Appl. Phys.* **2003**, *94* (3), 1795.

(18) Yu, D.; Feng, J.; Hone, J. *MRS Bull.* **2014**, *39* (02), 157−162.

(19) Mehl, B. P.; Kirschbrown, J. R.; House, R. L.; Papanikolas, J. M. *J. Phys. Chem. Lett.* **2011**, *2* (14), 1777−1781.

(20) Mehl, B. P.; Kirschbrown, J. R.; Gabriel, M. M.; House, R. L.; Papanikolas, J. M. *J. Phys. Chem. B* **2013**, *117* (16), 4390−4398.

(21) Gabriel, M. M.; Kirschbrown, J. R.; Christesen, J. D.; Pinion, C. W.; Zigler, D. F.; Grumstrup, E. M.; Mehl, B. P.; Cating, E. E.; Cahoon, J. F.; Papanikolas, J. M. *Nano Lett.* **2013**, *13* (3), 1336−40.

(22) Grumstrup, E. M.; Gabriel, M. M.; Cating, E. M.; Pinion, C. W.; Christesen, J. D.; Kirschbrown, J. R.; Vallorz, E. L.; Cahoon, J. F.; Papanikolas, J. M. *J. Phys. Chem. C* **2014**, *118* (16), 8634−8640.

(23) Gabriel, M. M.; Grumstrup, E. M.; Kirschbrown, J. R.; Pinion, C. W.; Christesen, J. D.; Zigler, D. F.; Cating, E. E.; Cahoon, J. F.; Papanikolas, J. M. *Nano Lett.* **2014**, *14* (6), 3079−87.

(24) Christesen, J. D.; Pinion, C. W.; Grumstrup, E. M.; Papanikolas, J. M.; Cahoon, J. F. *Nano Lett.* **2013**, *13* (12), 6281−6.

(25) Grumstrup, E. M.; Cating, E. M.; Gabriel, M. M.; Pinion, C. W.; Christesen, J. D.; Kirschbrown, J. R.; Vallorz, E. L.; Cahoon, J. F.; Papanikolas, J. M. *J. Phys. Chem. C* **2014**, *118* (16), 8626−8633.

(26) Sze, S. M.; Ng, K. K. *Physics of Semiconductor Devices*; John Wiley & Sons: New York, 2007.

(27) Li, C.-M.; Sjodin, T.; Dai, H.-L. *Phys. Rev. B* **1997**, *56* (23), 15252−15255.

(28) Allen, J. E.; Hemesath, E. R.; Perea, D. E.; Lensch-Falk, J. L.; Li, Z. Y.; Yin, F.; Gass, M. H.; Wang, P.; Bleloch, A. L.; Palmer, R. E.; Lauhon, L. J. *Nat. Nanotechnol.* **2008**, *3* (3), 168−73.

(29) Dan, Y.; Seo, K.; Takei, K.; Meza, J. H.; Javey, A.; Crozier, K. B. *Nano Lett.* **2011**, *11* (6), 2527−32.

(30) Munguía, J.; Bremond, G.; Bluet, J. M.; Hartmann, J. M.; Mermoux, M. *Appl. Phys. Lett.* **2008**, *93* (10), 102101.

(31) Henry, C.; Lang, D. *Phys. Rev. B* **1977**, *15* (2), 989−1016.